**IJCRT.ORG** 

ISSN: 2320-2882



# INTERNATIONAL JOURNAL OF CREATIVE RESEARCH THOUGHTS (IJCRT)

An International Open Access, Peer-reviewed, Refereed Journal

# IMPACT ON ZINC DOPING WITH LANTHANUM TITANATE NANOPARTICLES USING HYDROTHERMAL TECHNIQUE

<sup>1</sup>M. Vijaya Saritha, <sup>2</sup>MV Lakshmaiah, <sup>3</sup>S Dastagiri

<sup>1</sup>Research Scholar, Department of Physics, Sri Krishnadevaraya University, Ananthapuramu-515003, A.P.,India.

<sup>2</sup>Professor, Department of Physics, Sri Krishnadevaraya University, Ananthapuramu-515003, A.P.,India. <sup>3</sup>Academic Consultant,Department of Physics, Sri Krishnadevaraya University, Ananthapuramu-515003, A.P.,India.

Abstract: This study focuses on the synthesis and characterization of Zn<sub>x</sub>La<sub>1-x</sub>TiO<sub>3</sub> (x = 0.1 - 0.7) (ZLTO) nanoparticles. X-ray diffraction patterns confirmed the tetragonal structure and phase purity, with unit cell dimensions expanding as Zn content increased. Morphological analysis revealed the formation of spherical grains, rods, and nanoscale particles. UV-Visible spectroscopy indicated a band gap (E<sub>g</sub>) ranging from 3.01 eV to 3.64 eV, depending on the value of 'x'. The frequency and compositional dependence of dielectric parameters were also examined. Space charge polarization was effectively analyzed using complex dielectric modulus and impedance spectroscopy. Cole-Cole plots confirmed the semiconducting nature of ZLTO materials, evidenced by the complete semicircular arcs, and revealed the presence of non-Debye type relaxations.

Keywords: Nanoparticles; Hydrothermal; Structure; Morphology; Band Gap; Dielectrics.

# 1.Introduction

Perovskite materials typically follow the general chemical formula ABO<sub>3</sub>, where the A and B-site cations can have varying valencies depending on the stability of the compound [1]. In some cases, the A-site cation may be divalent or trivalent, while the B-site cation is typically tetravalent. These perovskite materials have garnered significant attention in recent decades due to their diverse structural, optical, morphological, electrical, ferroelectric, piezoelectric, physical, and chemical properties [2-4]. Among these, LaTiO<sub>3</sub> (LT) stands out as a promising material exhibiting several of these properties. Extensive research has been conducted on LT in both its bulk and nanostructured forms. For example, Madhavan et al. [5] synthesized LT via the sol-gel method and investigated the effects of A and B-site doping on its dielectric constant, finding that A-site doping resulted in a dielectric constant of 1500, while B-site doping achieved a value of 900 at 100 Hz. Similarly, Mozhegorov et al. [6] and Ishida et al. [7] studied the bulk LT, focusing on its orbital structure and electronic properties, respectively. Other researchers have explored various properties of LT material [8-11]. Additionally, LT materials doped with elements such as Ag, Cu, Au, N, Sr, Ba, and Ca, in forms ranging from bulk to nanoparticles, nanocomposites, thin films, and polymers, have been extensively studied to examine their structural, optical, physical, magnetic, electrical, ferroelectric, piezoelectric, and other chemical properties [12-22]. In a similar vein, zinc titanate has been synthesized to evaluate its photocatalytic, biomedical, electrical, and physical properties [23-27], with findings confirming its tetragonal structure. A review of the literature reveals that research on Zn-doped LT, particularly concerning its structural, morphological, optical, and electrical properties, is quite limited. Therefore, this study aims to investigate these properties through the synthesis and characterization of  $Zn_xLa_{1-x}TiO_3$  (x = 0.1 - 0.7) nanoparticles using the cost-effective hydrothermal method.

#### 2. MATERIAL AND EXPERIMENTAL METHODS

A series of  $Zn_xLa_{1-x}TiO_3$  (x = 0.1, 0.3, 0.5, and 0.7) nanoparticles were synthesized through the hydrothermal method. The preparation process is illustrated in Figure 1. The starting materials used were Zn (NO<sub>3</sub>)<sub>2</sub>·6H<sub>2</sub>O (99.8% purity, Sigma-Aldrich), La(NO<sub>3</sub>)<sub>3</sub>·6H<sub>2</sub>O (99.8% purity, Sigma-Aldrich), and TiO<sub>2</sub> (99.9% purity, Sigma-Aldrich), which were accurately measured based on the stoichiometric formula using a precise digital scale. Zinc nitrate, lanthanum nitrate, and titanium dioxide were dissolved in distilled water in a 1:3 ratio. Sodium hydroxide (NaOH) was then gradually added to the mixture, adjusting the pH to between 9 and 12. The resulting solution was transferred into a 500 mL Teflon-lined stainless-steel autoclave, which was subsequently placed in a hot-air oven and heated at 160°C for 8 hours. After the reaction, the autoclave was allowed to cool to room temperature. The synthesized ZLTO nanoparticles were removed from the autoclave and rinsed with acetone and distilled water until the pH of the solution reached 7. The final product was then finely ground and subjected to heat treatment for one hour. The ZLTO powder was characterized using several analytical techniques: X-ray diffraction (Bruker X-ray Powder Diffractometer,  $CuK_{\alpha}$  radiation,  $\lambda = 0.15406$  nm) for structural analysis, Transmission Electron Microscopy (TEM: Tecnai G20, FEI, USA) and Field Emission Scanning Electron Microscopy (FE-SEM: Ultra 55, Carl Zeiss) for morphological studies, JASCO UV-Visible spectrophotometer (V-670 PC) for band gap analysis, and an LCR meter (HIOKI 3532-50) for examining electrical properties.

# 3. RESULTS AND DISCUSSIONS

# 3.1. X-RAY DIFFRACTION ANALYSIS

The X-ray diffraction (XRD) spectra of ZLTO nanoparticles, as shown in Fig. 1, exhibit variations in intensity across different two-theta angles, confirming the crystallinity of all compositions. The average crystallite size (D) was calculated using the Scherrer equation [28], revealing an increase in D from 24.11 nm to 28.58 nm as the Zn content (x) varied from 0.1 to 0.7. This trend may be attributed to the intrinsic microstrain generated during the hydrothermal synthesis [1]. The (103) plane exhibited the highest diffraction counts, and the observed diffraction peaks were matched with the standard JCPDS: 89-7507, confirming that the indexed planes correspond to a tetragonal structure. Lattice parameters (a = b & c) were computed using the standard formula  $1/d^2 = (h^2 + k^2)/a^2 + l^2/c^2$ , where 'd' is the interplanar distance and (hkl) are the Miller indices. The calculated lattice constants increased from 3.843 Å to 3.921 Å for a = b, and from 27.176 Å to 27.718 Å for c, with the changes corresponding to varying dopant concentrations. Consequently, the unit cell volume ( $V = a^2c$  for a tetragonal unit cell) expanded from 401.353 Å<sup>3</sup> to 426.143 Å<sup>3</sup>, while the full-width at half maximum (FWHM) in radians decreased from 0.08715 to 0.08077. The variation in lattice constants can be understood through Shannon ionic radii data [29], which shows La<sup>3+</sup> has a radius of 0.136 nm, Zn<sup>2+</sup> has 0.074 nm, and Ti<sup>4+</sup> has 0.068 nm. The smaller ionic radius of Zn<sup>2+</sup> compared to La<sup>3+</sup> suggests that Zn<sup>2+</sup> might replace La<sup>3+</sup> in the lattice, leading to a contraction of the unit cell and an increase in dimensions and volume. Although Zn<sup>2+</sup> could potentially occupy Ti<sup>4+</sup> sites, this is unlikely due to the different valencies. In cases where Ti<sup>3+</sup> is present, oxygen excess or deficit may occur, resulting in a neutralized tetragonal structure such as  $Zn_xLa_{1-x}TiO_{3+\delta}$ , as noted in the literature [30]. The tetragonal phase was also reported for Zn-doped TiO<sub>2</sub> [23], indicating that the presence of La did not alter the phase structure. The X-ray density ( $\rho_x$ ) was calculated using  $\rho_x = ZM/Na^2c$  for a tetragonal structure, where 'M' is the molecular weight (see Table 1), 'N' is Avogadro's number  $(6.023 \times 10^{23})$ , and 'a' and 'c' are the lattice parameters. The density decreased from 3.7631 g/cm<sup>3</sup> to 2.8566 g/cm<sup>3</sup>, reflecting the reduction in density with increasing Zn content due to the decrease in molecular weight. The surface area (S) of the samples was determined using the formula  $S = 6000/(D*\rho_x)$ , where D is the average crystallite size and  $\rho x$  is the density. The surface area increased from 66.131 m<sup>2</sup>/g to 73.489 m<sup>2</sup>/g for Zn contents x = 0.1 to 0.7, which is proportional to the average crystallite size [30]. This variation in surface area impacts various functional properties of the ZLTO materials.

# 3.2.SURFACE MORPHOLOGY

The surface morphology of ZLTO nanomaterials was analyzed using FESEM and TEM micrographs. Figure 2 displays FESEM images for compositions x=0.1–0.7. These images reveal that all Zn contents resulted in the presence of numerous nanospheres and nanorods. Notably, the x=0.5 sample exhibited a few rod-like grains, likely due to the high La content, consistent with similar observations reported in the literature [3, 8]. In contrast, increased Zn content ( $x=0.1,\ 0.3,\ \&\ 0.7$ ) resulted in well-defined nanospheres with a homogeneous distribution. The average grain size ( $G_a$ ) was determined using the linear intercept method. Ten test lines with varying lengths (L) were drawn for each composition at a specific magnification (M) and working distance (WD), and the number of intersecting grains (N) was counted. These parameters were used in the formula  $G_{avg}=1.5L/MN$  to calculate the experimental grain size. The results showed a decrease in grain size from 149.775 nm to 128.37 nm for x=0.1–0.5, with an increase to 154.195 nm for x=0.7.

TEM images, shown in Figure 3, also displayed well-defined nanospheres with a homogeneous distribution across all samples.

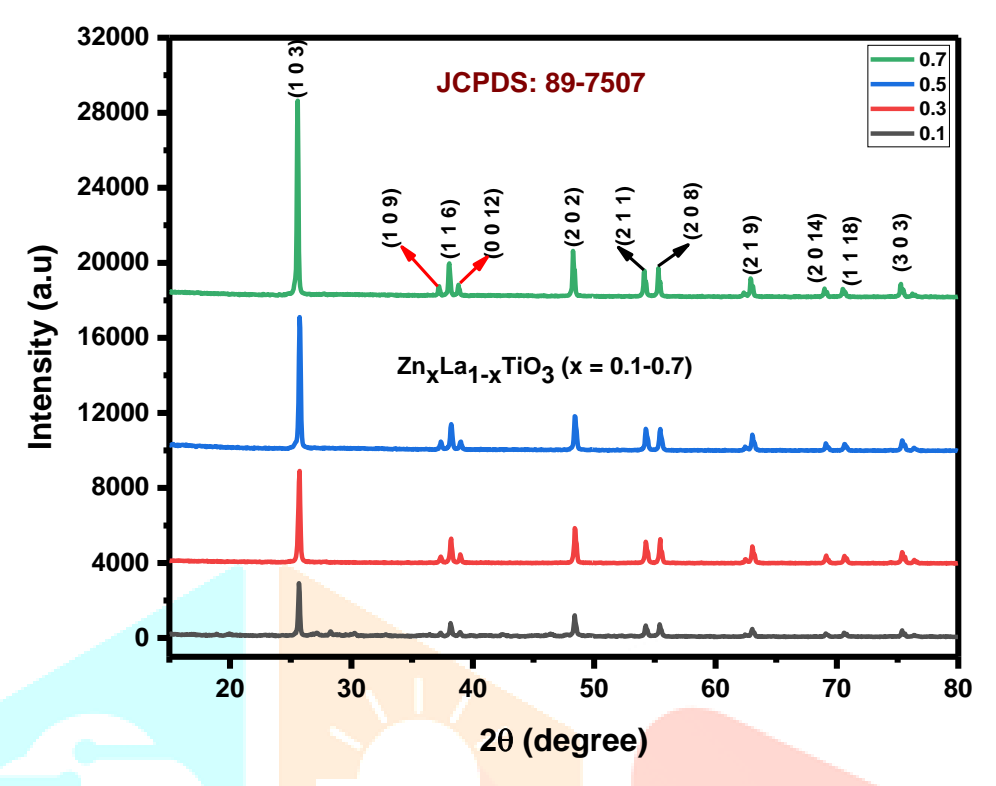
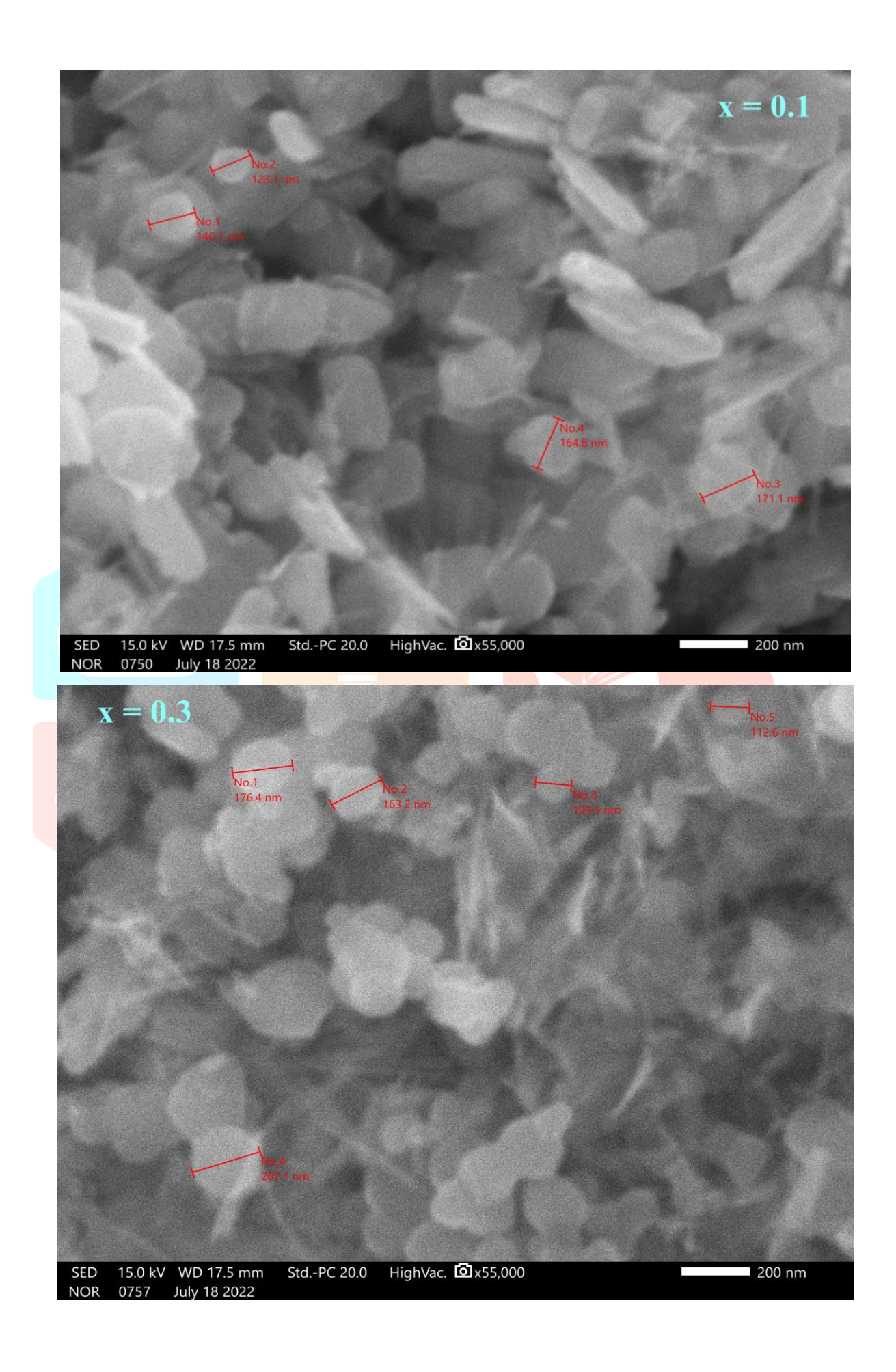


Fig.1 XRD patterns of ZLTO samples

For the x = 0.5 composition, nanorod-like particles were not observed, likely due to the focus being limited to a selected portion of the powder sample. The average particle size  $(P_a)$  was calculated and decreased from 73.126 nm to 57.508 nm for x = 0.1-0.5, but increased to 85.285 nm for x = 0.7. Additionally, the selected area electron diffraction (SAED) patterns for x = 0.1-0.7, presented in Figure 4, showed well-defined rings corresponding to the tetragonal reflection planes, indicating good crystallinity. These patterns corroborate the XRD diffraction results.

Table. 1 Data on structural and physical parameters of ZLTO nanoparticles

x	0.1	0.3	0.5	0.7
a=b (A <sup>0</sup> )	3.843	3.874	3.904	3.921
c (A <sup>0</sup> )	27.176	27.396	27.602	27.718
c/a	7.07155	7.07176	7.07018	7.06911
Dave (nm)	24.11	25.76	27.32	28.58
FWHM in radians	0.08715	0.08631	0.08429	0.08077
Volume V (A <sup>03</sup> )	401.353	411.156	420.688	426.143
MW g/mol	227.418	212.713	198.008	183.303
Surface Area S (m²/g)	66.131	67.791	70.278	73.489
X-ray Density ρ <sub>x</sub> (g/cm <sup>3</sup> )	3.7631	3.4358	3.1258	2.8566
Dislocation density $\rho(m^{-2})$	1.7203E+15	1.5069E+15	1.3398E+15	1.1118E+15
G <sub>a</sub> (nm)	149.775	152.96	128.37	154.195
P <sub>a</sub> (nm)	73.126	64.096	57.508	85.285



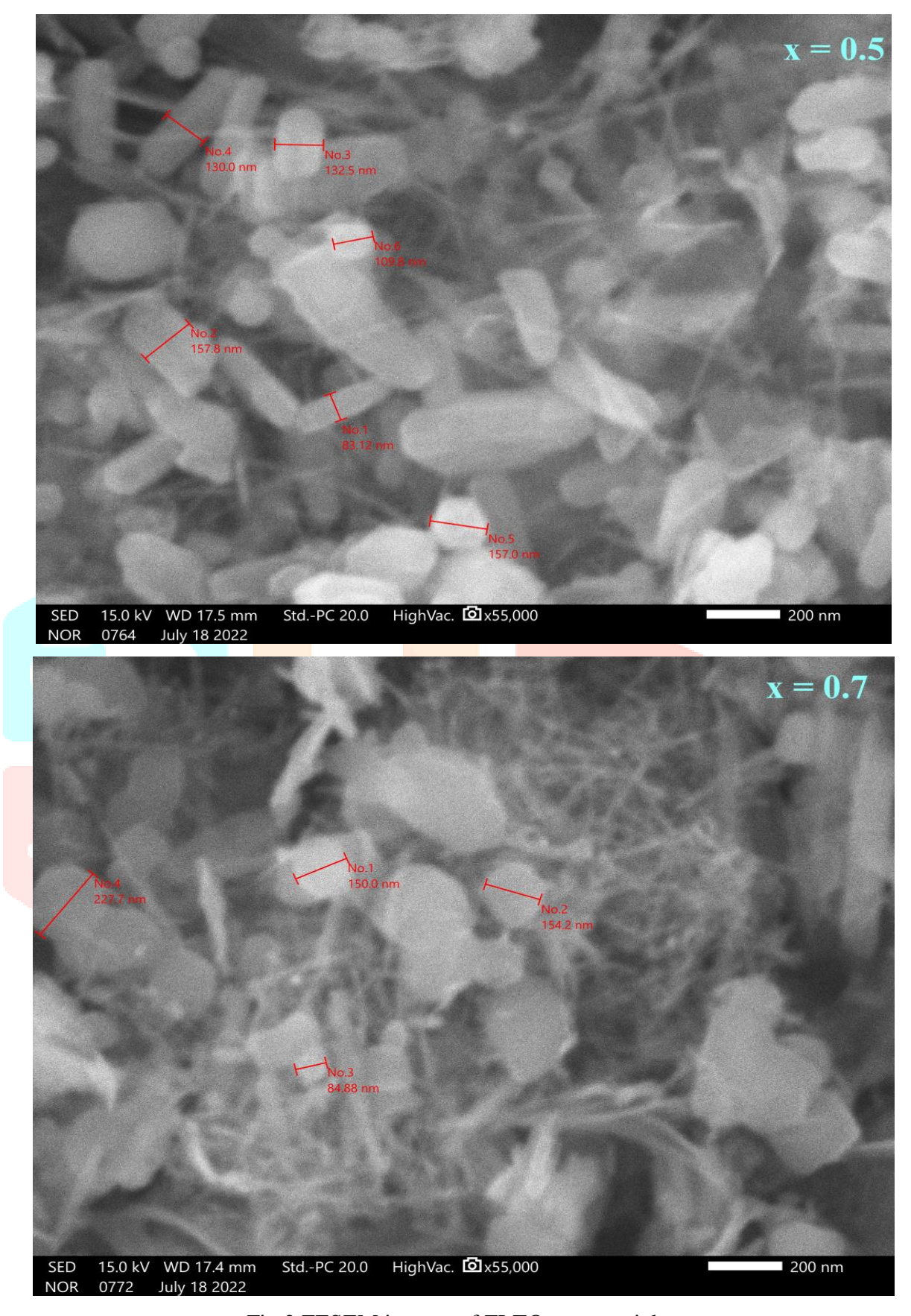
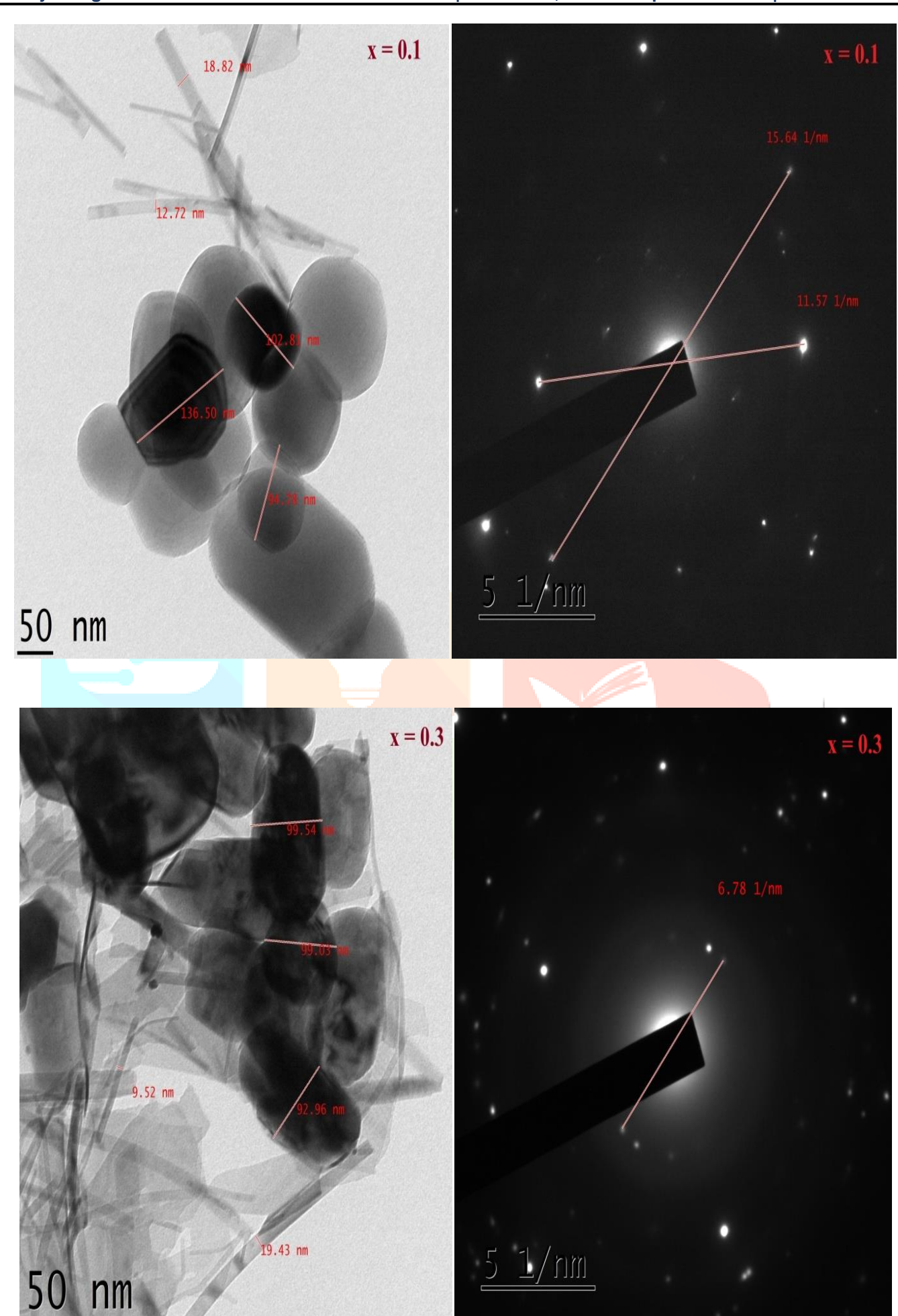


Fig.2 FESEM images of ZLTO nanoparticles



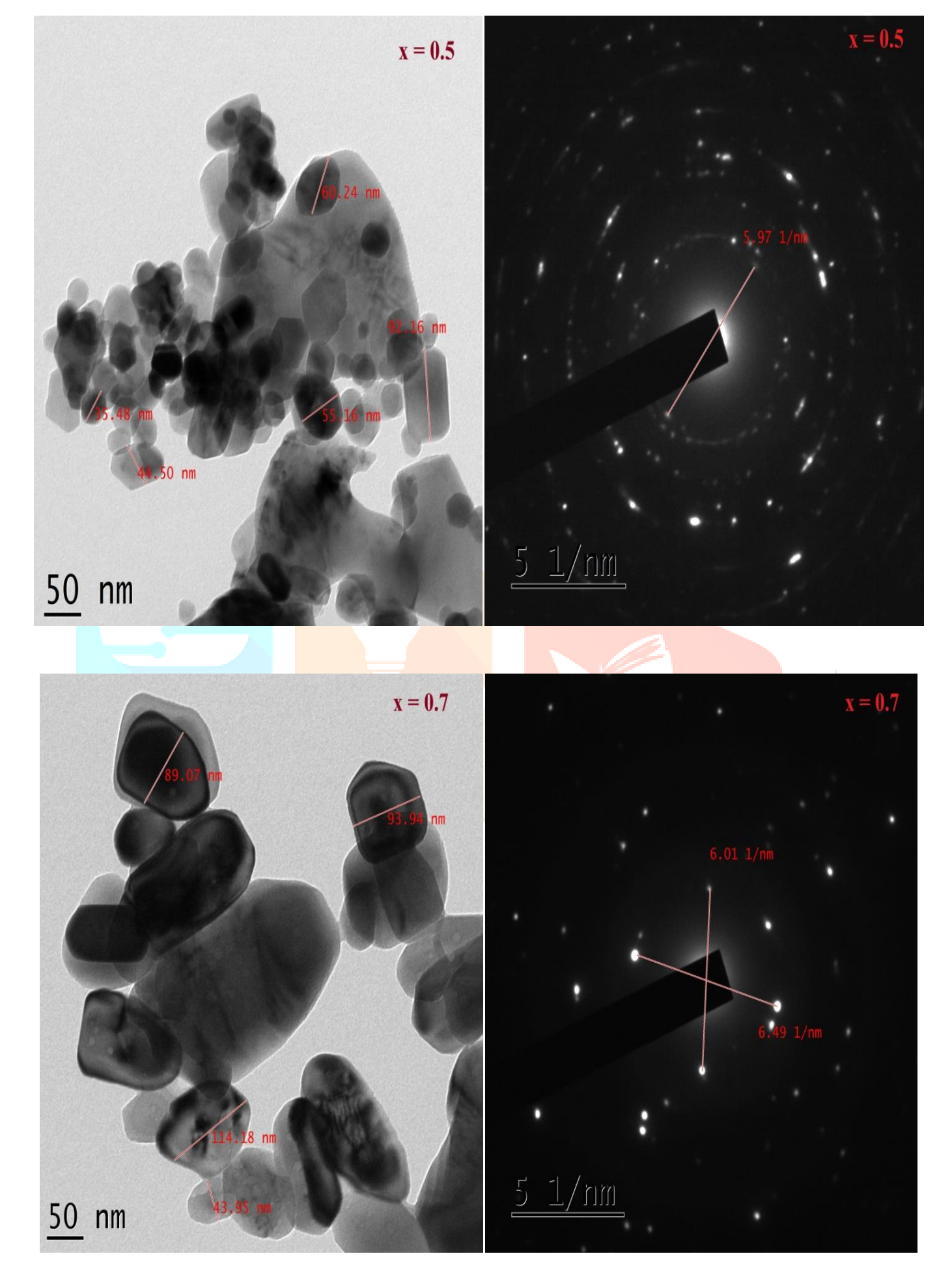
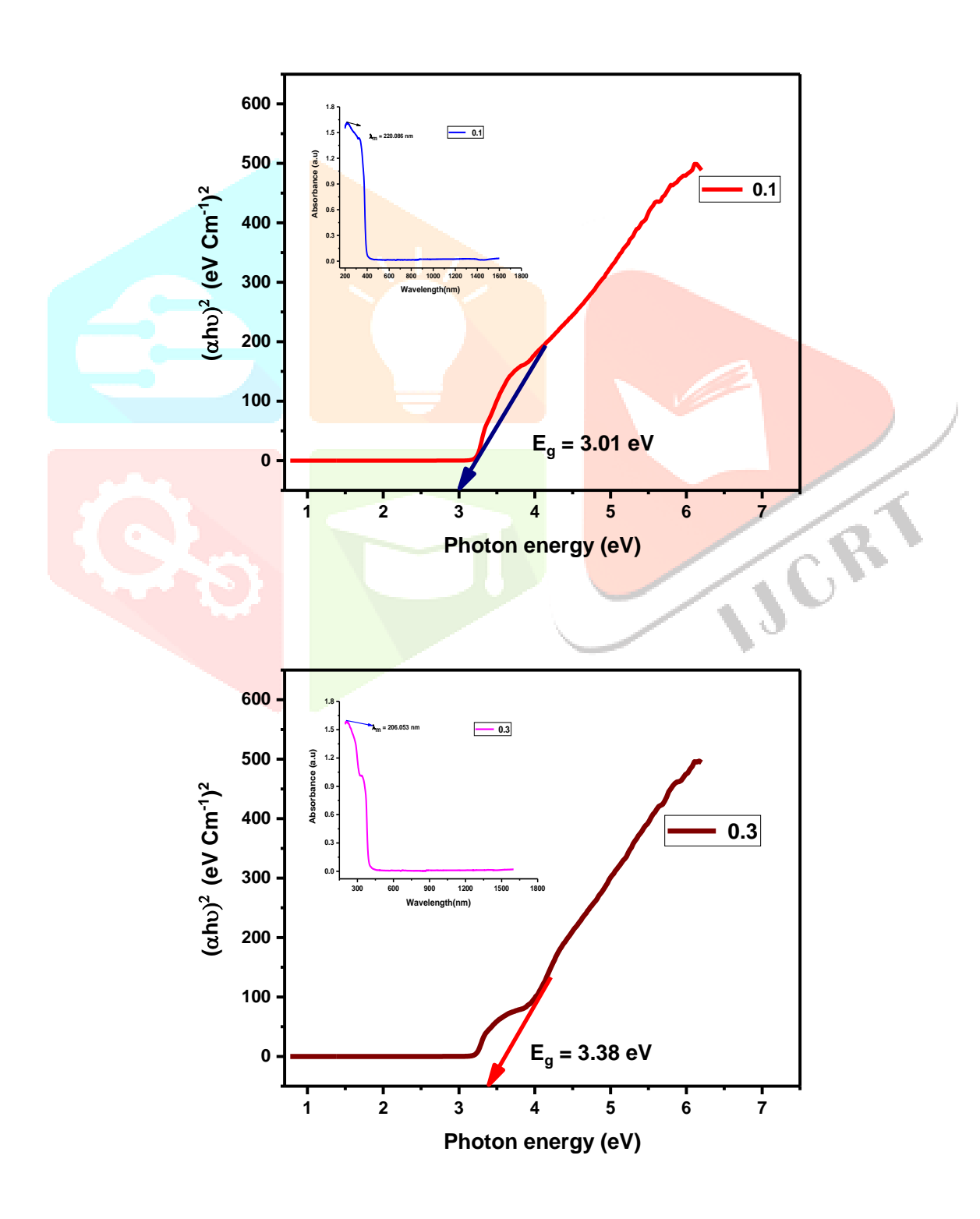


Fig.3 TEM and SAED images of ZLTO nanoparticles

#### 3.3.UV-VISIBLE SPECTRA ANALYSIS

The optical band gap ( $E_g$ ) of ZLTO nanoparticals was determined for various Zn contents using the diffuse reflectance spectra (see inset of Fig. 4). To achieve this,  $(\alpha h \upsilon)^2$  versus h $\upsilon$  plots were generated, where ' $\alpha$ ' represents absorptivity and 'h $\upsilon$ ' is the photon energy, with n=2. The choice of n=2 corresponds to a direct electronic transition between energy bands [30]. Analysis of the  $(\alpha h \upsilon)^2$  versus h $\upsilon$  plots revealed that the  $E_g$  values ranged from 3.01 eV to 3.64 eV for Zn contents (x) varying between from 0.1 to 0.7. This indicates that the Zn content significantly affects the  $E_g$  value. The  $E_g$  values were calculated by extrapolating the linear portion of the plots (Fig. 4) to the photon energy axis, where the absorptivity becomes zero [30-32]. For comparison, reference [33] reports band gaps of ZTO samples calcined at different temperatures (500-800°C) ranging from 3.31 eV to 3.55 eV. However, in the current study, the presence of La resulted in a higher  $E_g$  value, from 3.01 eV to 3.64 eV. These wide band gap materials are thus promising candidates for sensor device applications [30-34].



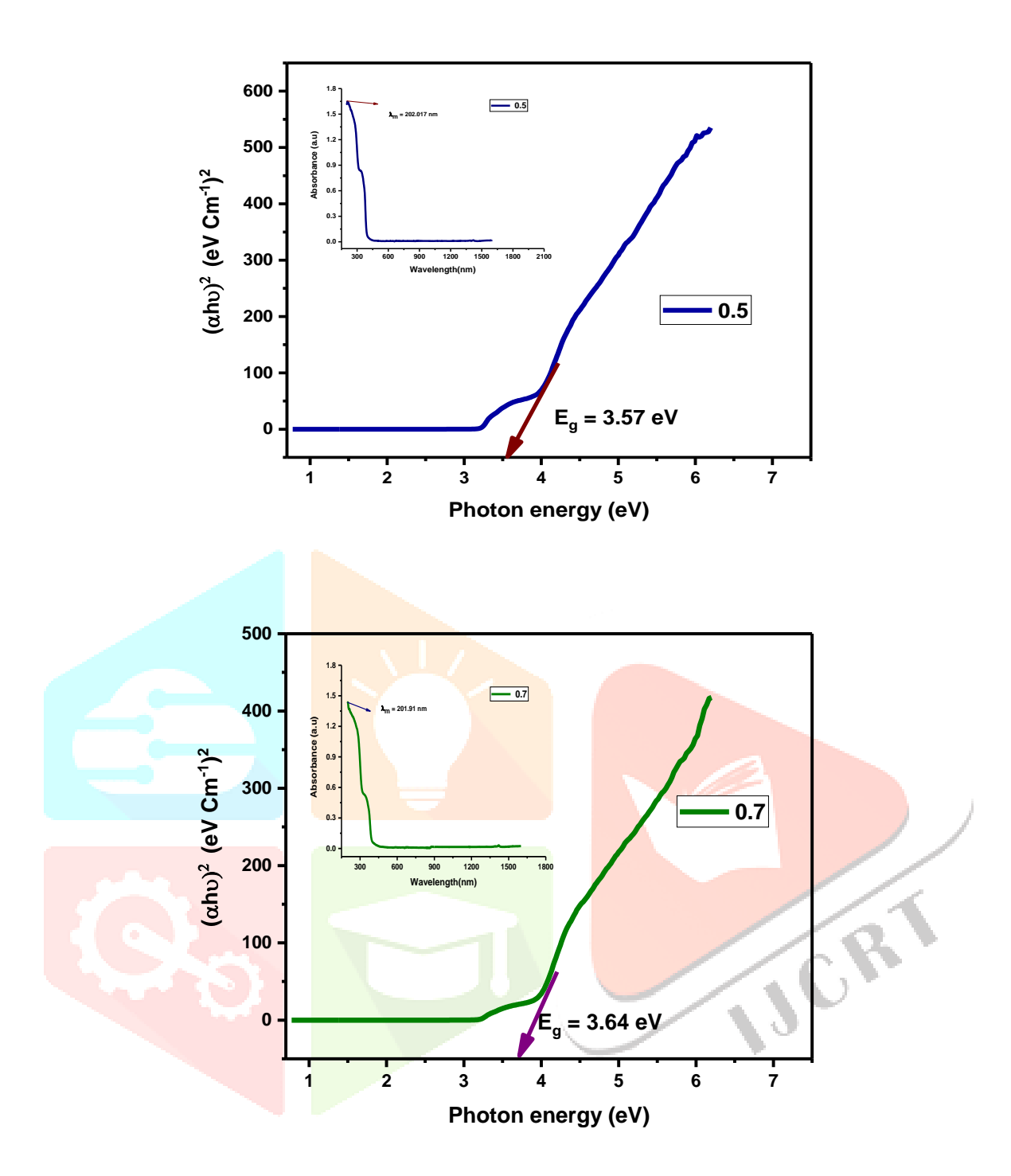


Fig.4. The Energy bandgap values of ZLTO nanoparticles

# 3.4.FTIR SPECTRA ANALYSIS

The Fourier transform infrared (FTIR) spectra of ZLTO nanoparticles were recorded over a wave number range of 4000–400 cm<sup>-1</sup>, as illustrated in Fig. 5. The A and B-site locations were identified using the  $\nu_a$  and  $\nu_b$  peaks, which indirectly suggest the formation of a perovskite structure. The  $\nu_a$  and  $\nu_b$  peaks were observed in the ranges of 540 to 550 cm<sup>-1</sup> and 447 to 457 cm<sup>-1</sup>, respectively. These absorption bands,  $\nu_a$  and  $\nu_b$ , indicate the presence of metal oxide (M–O: Zn–O, La–O, Ti–O) stretching vibrations [35]. Additionally, bands in the 764 to 781 cm<sup>-1</sup> range were also associated with metal oxide bonds characteristic of the parent perovskite structure. Peaks observed in the 1389–1414 cm<sup>-1</sup> and 3563–3617 cm<sup>-1</sup> ranges were attributed to the O–H stretching and bending vibrations of H<sub>2</sub>O molecules absorbed by the ZLTO nanoparticles [35], suggesting that moisture had a slight influence on the material.

#### 3.5.DIELECTRIC PROPERTIES

The dielectric properties of ZLTO nanoparticles were examined by analyzing the dielectric constant ( $\epsilon$ ') and dielectric loss ( $\epsilon$ ") across a frequency range from 100 Hz to 5 MHz, as shown in Fig. 6. Figure 6(a) demonstrates that  $\epsilon$ ' values are higher at low frequencies and decrease at high frequencies. A similar pattern

is observed in the  $\varepsilon''$  versus log f plots (Fig. 6(b)). This behavior can be explained by Koop's theory, also known as the double layer theory [30]. According to this theory, a

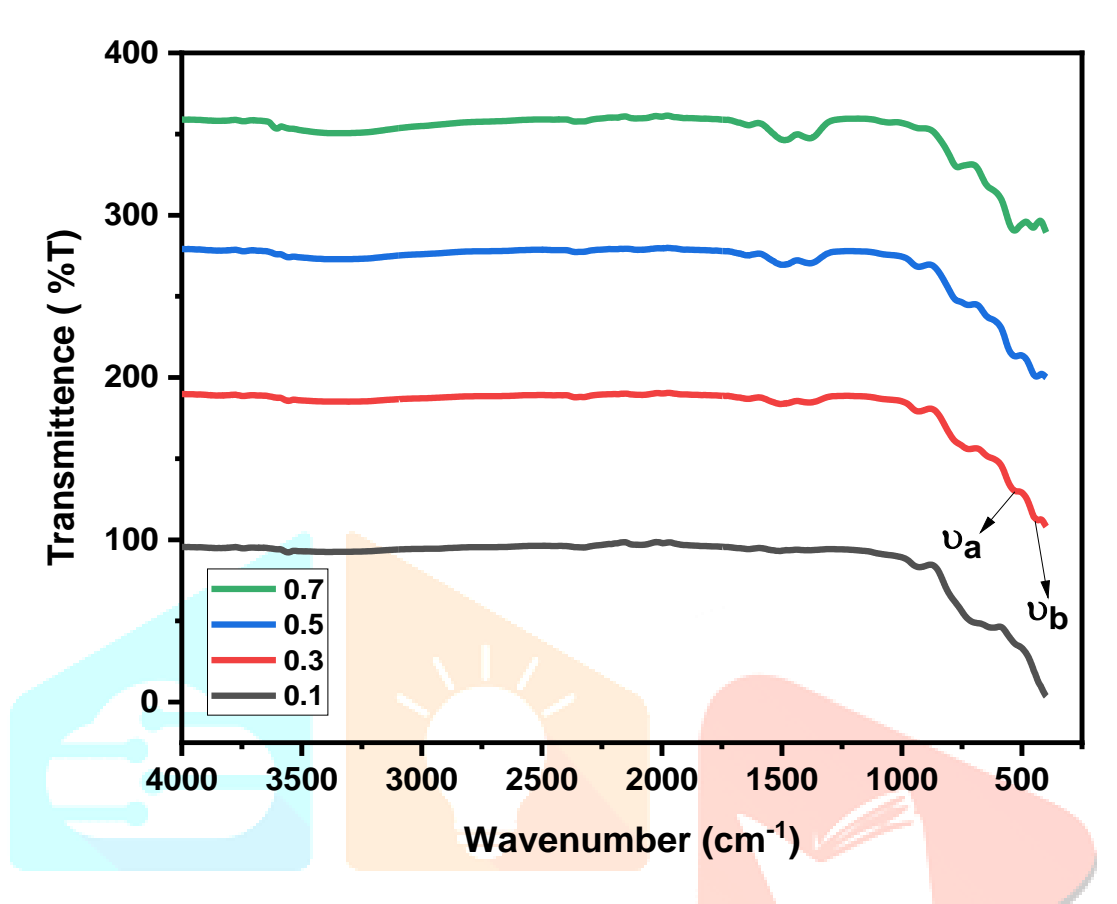
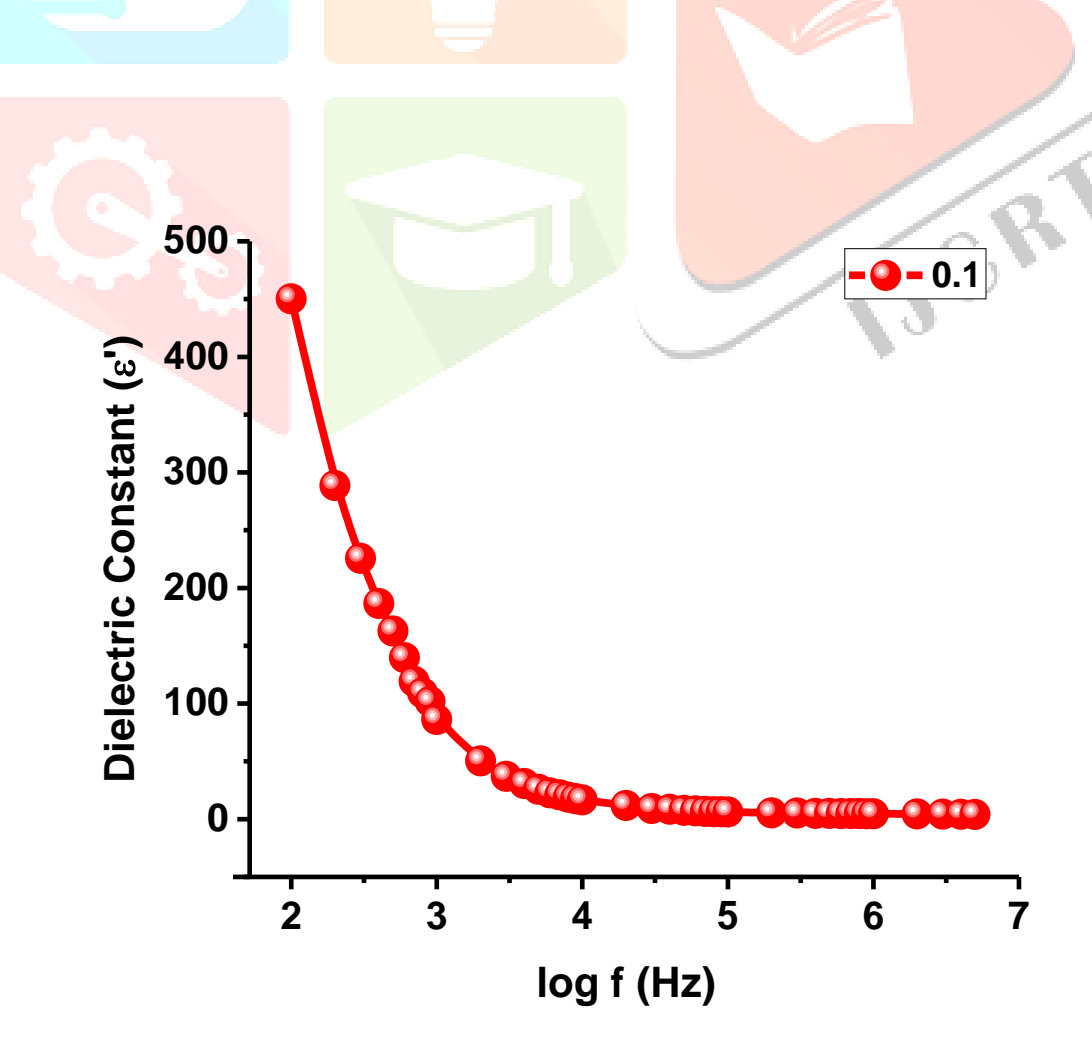


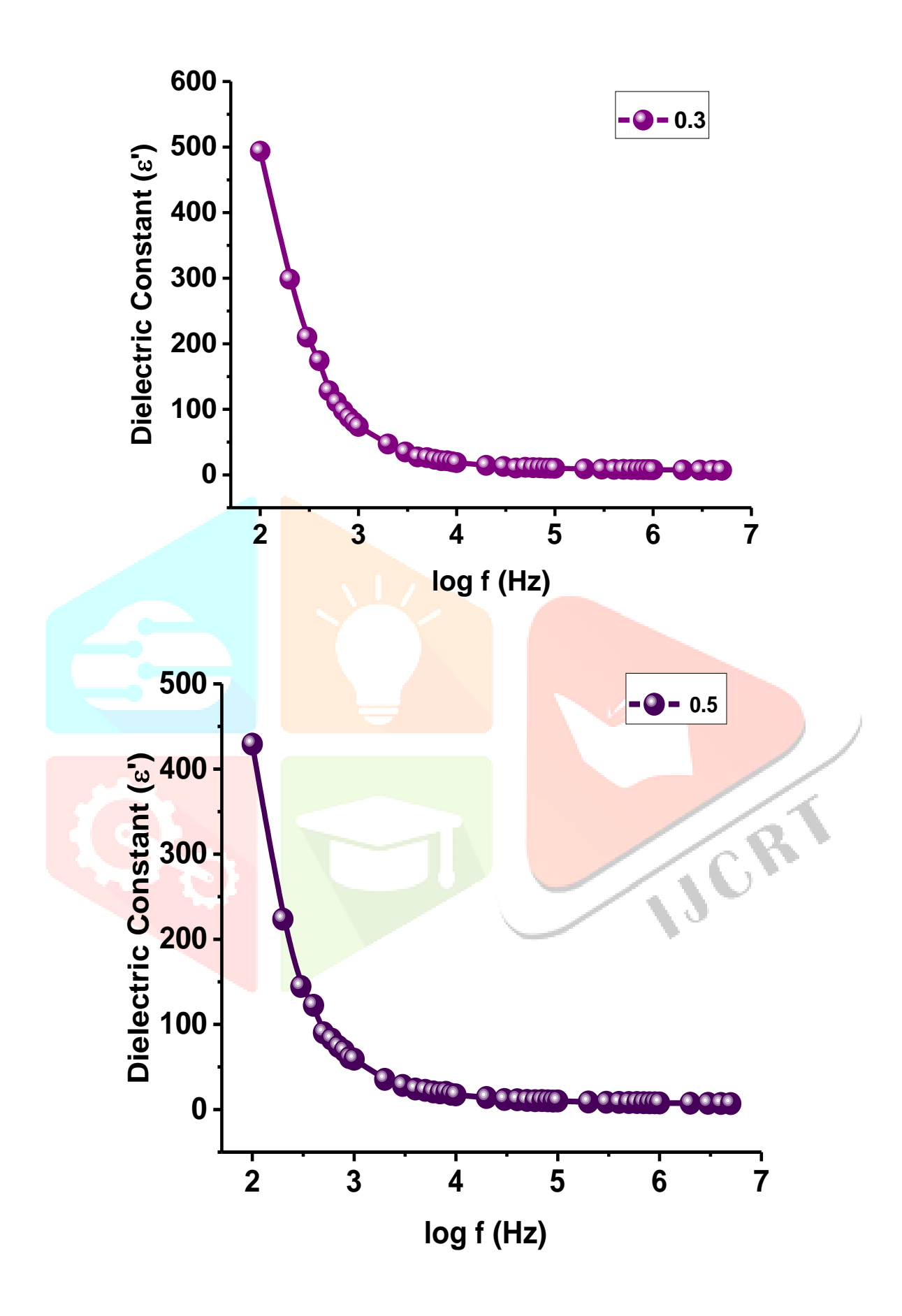
Fig.5 FTIR Spectra of ZLTO nanoparticles

polycrystalline material is composed of two regions: the grains and the grain boundaries, with the latter being more resistive. At low frequencies, charge carriers are fully activated and move towards the grain boundary, leading to a higher accumulation of charge at the interfaces. This accumulation enhances Maxwell-Wagner interfacial or space charge polarization, resulting in higher  $\varepsilon'$  and  $\varepsilon''$  values at low frequencies [31]. However, at higher frequencies, the effectiveness of space charge polarization decreases, leading to reduced  $\varepsilon'$  and  $\varepsilon''$  values, as evidenced in Fig. 6. This trend is consistent with findings from previous studies [32-39]. Additionally, the frequency dependence of  $\varepsilon'$  and  $\varepsilon''$  shows non-Debye type relaxations across the frequency range from 100 Hz to 5 MHz. This non-Debye behavior typically occurs when the frequency of the applied electric field matches the oscillation frequency of the electric dipoles [3]. Numerical values for  $\varepsilon'$  and  $\varepsilon''$  are listed in Table 2. Specifically,  $\varepsilon'$  ranged from 4.07183 to 7.7316 at 5 MHz for x = 0.1 to 0.7, while  $\varepsilon''$  ranged from 0.3540 to 0.8528 at 5 MHz for the same composition range. These results support the adherence of ZLTO nanomaterials to the double layer model. The log  $\sigma_{ac}$  versus log  $\omega$ plots depicted in Fig. 7 illustrates the relationship between electrical conductivity and angular frequency. The plots reveal that as the angular frequency increases, the ac-electrical conductivity also rises. This behavior is attributed to the thermally activated charge carriers, which become more prominent with the increase in log ω. These charges contribute to the electrical conduction through a hopping mechanism between cations of the same type but with different valencies [40]. This increase in conductivity is typically due to the rapid electron hopping between these cations. Additionally, the  $\sigma_{ac}$  values for ZLTO at various frequencies are presented in Table 3. The results ensure  $\sigma_{ac}$  values vary between from 3.586E-08 to 5.117E-08 at 100Hz and 1.691E-06 to 9.849E-07 at 5MHz. The data shows moderate  $\sigma_{ac}$  values, which can be linked to a relatively slower electron hopping process.

Table. 2. Data on dielectric constant and dielectric loss of ZLTO nanoparticles

X	0.1	0.3	0.5	0.7		
ε' at different frequencies						
100 Hz	450.1369	493.6837	429.2485	328.1503		
1 kHz	86.2176	73.9206	59.0499	47.3267		
10kHz	16.5698	18.7493	17.2901	19.6751		
0.1 MHz	6.1096	10.0735	10.0112	10.6996		
1 MHz	4.6298	7.9763	7.7951	9.0332		
5 MHz	4.07183	7.0600	6.9399	7.7316		
ε" at different frequencies						
100 Hz	762.1988	919.7327	885.0246	644.6446		
1 kHz	139.4131	95.8641	68.5541	37.7904		
10kHz	14.4719	10.6766	8.7989	8.3149		
0.1 MHz	2.1187	2.5073	2.6182	2.0594		
1 MHz	0.5747	1.0058	0.8088	1.2892		
5 MHz	0.3540	0.6740	0.6078	0.8528		





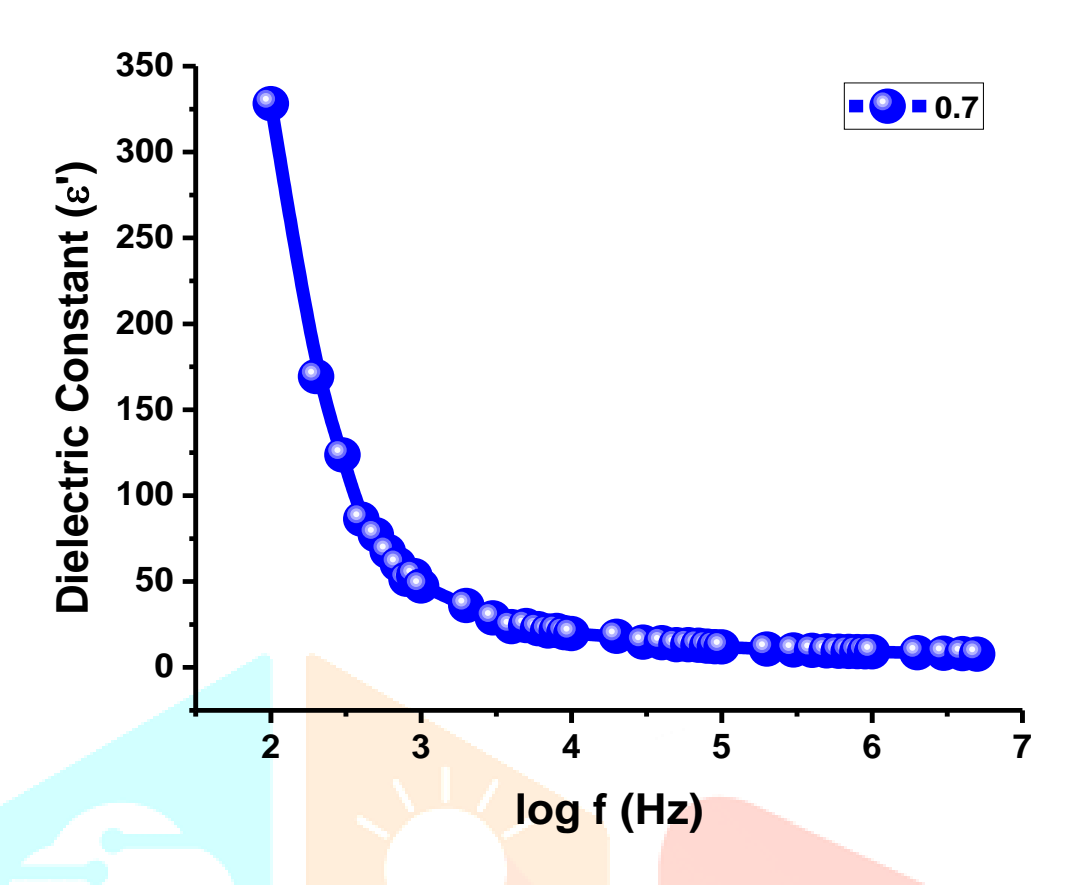
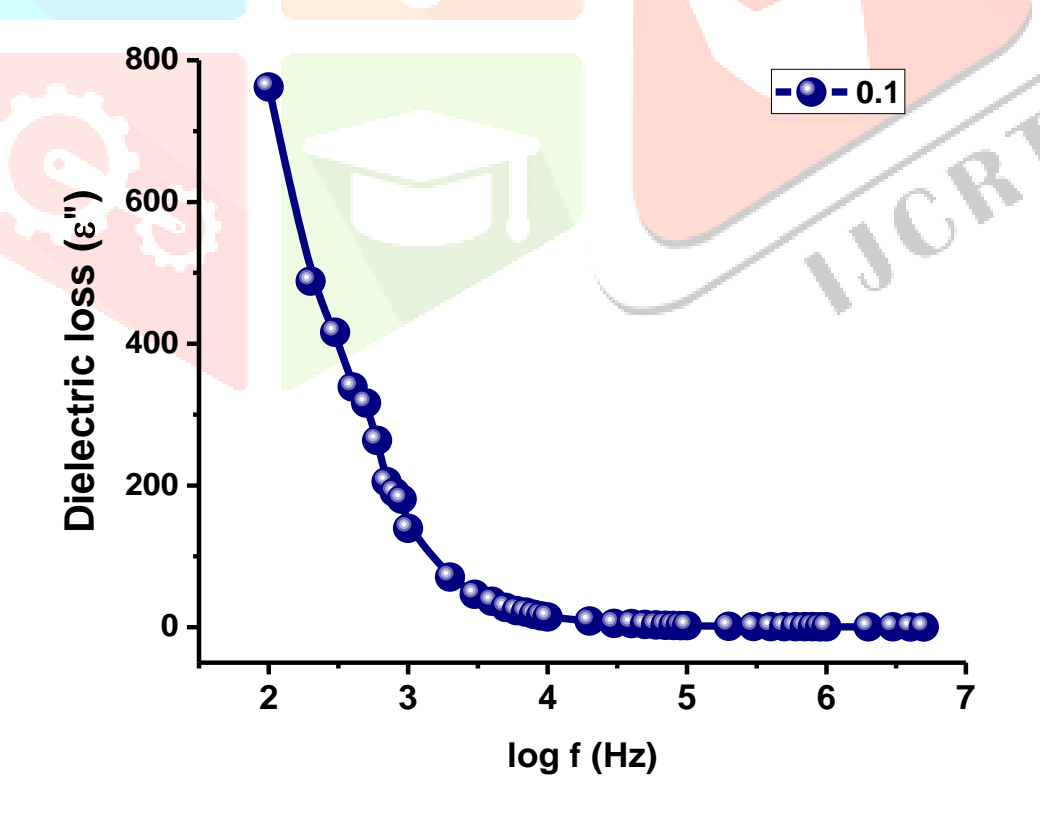
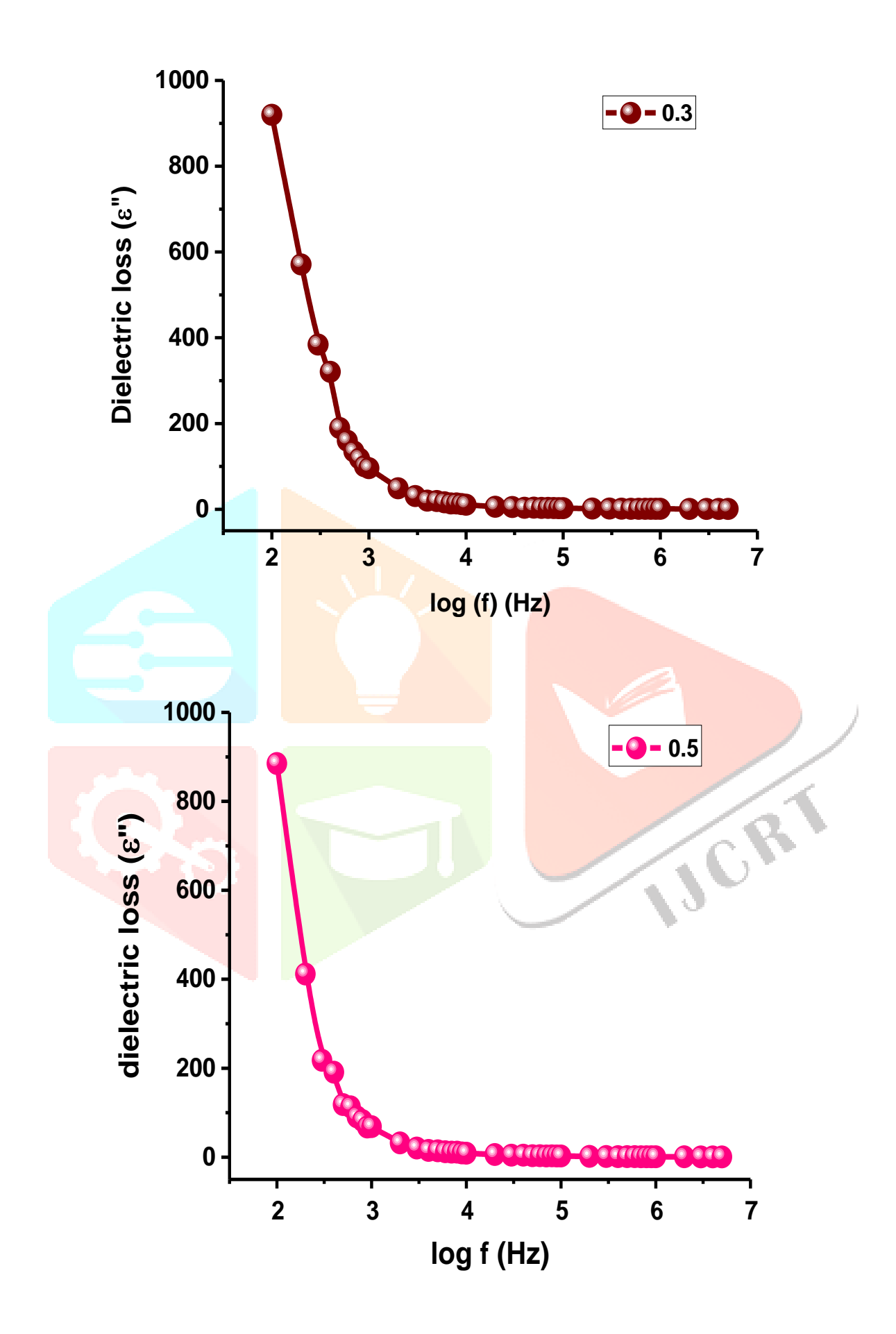


Fig. 6 a. Dielectric constant of ZLTO nanoparticles





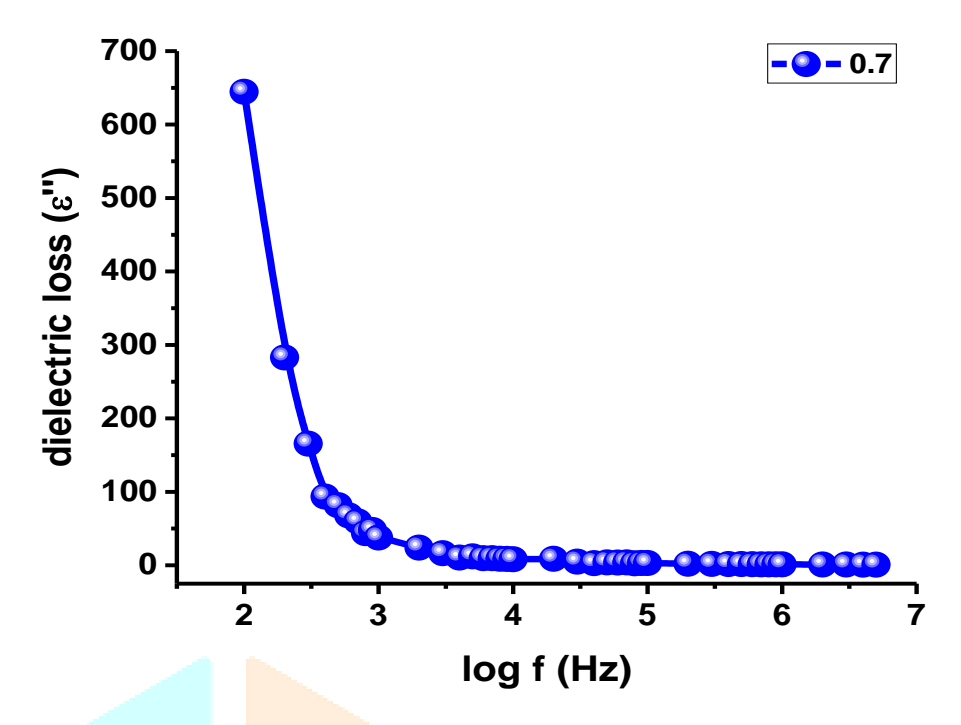


Fig. 6 b. Dielectric loss of ZLTO nanoparticles

Table 3. Data on  $\sigma_{ac}$  of ZLTO nanoparticles

X	0.1	0.3	0.5	0.7			
σ <sub>ac</sub> at different frequencies							
100 Hz	4.241E-08	5.117E-08	4.924E-08	3.586E-08			
1k Hz	7.756E-08	5.334E-08	3.814E-08	2.103E-08			
10k Hz	8.052E-08	5.940E-08	4.895E-08	4.626E-08			
0.1M Hz	1.178E-07	1.395E-07	1.456E-07	1.752E-07			
1M Hz	3.197E-07	5.596E-07	4.500E-07	7.173E-07			
2M Hz	4.806E-07	8.347E-07	7.375E-07	1.098E-06			
3M Hz	6.613E-07	1.171E-06	1.071E-06	1.601E-06			
4M Hz	8.225E-07	1.507E-06	1.367E-06	1.936E-06			
5M Hz	9.849E-07	1.875E-06	1.691E-06	2.372E-06			

Dielectric modulus parameters, including the real part (M') and the imaginary part (M"), provide valuable insights into space charge polarization and relaxation mechanisms [34]. The frequency dependence of M' and M" is depicted in Fig. 8a. The figure shows that both M' and M" approach nearly zero at low log f values. This is due to the long-range motion of charge carriers, which lack sufficient restoring force to return to their original positions [33]. As the frequency increases, M' and M" rise, reaching their maximum values. This increase is attributed to the carriers' movement over shorter distances [33]. For compositions x = 0.1 to 0.7, M'-log f plots reveal minor relaxation dynamics, with log f values decreasing from 4.642 to 4.289. Similarly, M"-log f plots show small relaxations with log f values decreasing from 4.687 to 4.297. Significant relaxation behaviors are observed, indicating non-Debye type relaxations. These relaxations result from the accumulation of mobile charge carriers at the grain boundaries and their tendency to align with the electric field [34]. Consequently, small M" values are observed at the relaxation peaks. The long-

range and short-range polarization mechanisms are evident before and after the relaxation frequencies, respectively.

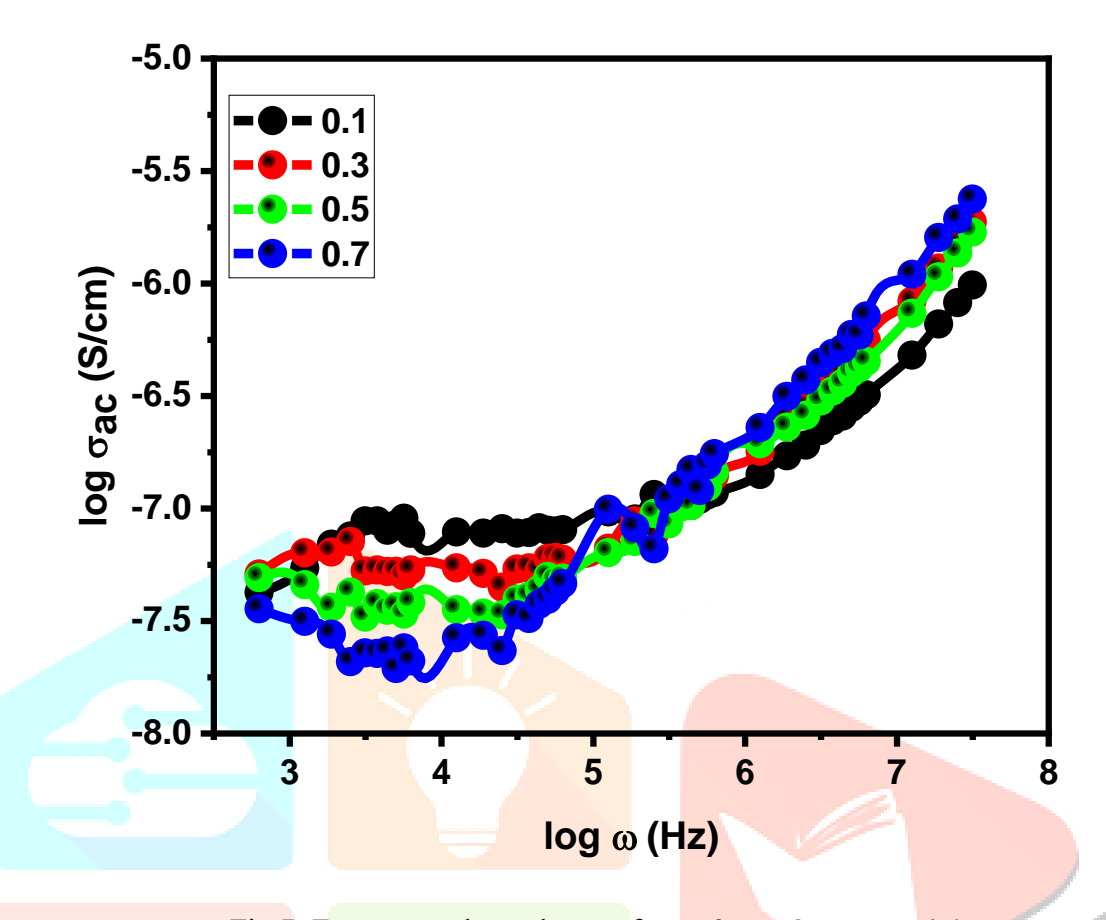


Fig. 7. Frequency dependence of  $\sigma_{ac}$  of ZLTO nanoparticles

Long-range carrier mobility supports long-range conduction, while short-range carrier mobility leads to short-range conduction [33]. Fig. 8b presents M' versus M" plots, where x = 0.1 shows single semicircular arcs, while x = 0.7 exhibits some distortions. These distortions are typically due to factors such as grain size, defects, microstrain, porous structure, and moisture [34]. For x = 0.1, the plots indicate significant grain contribution due to nanoparticles within the microstructure. Similar trends are observed in the Cole-Cole plots (M' versus M" plots). Notably, x = 0.3 and x = 0.5 show two distinct arcs in each plot, reflecting the microstructural behavior. In these compositions, the presence of spherical grains and numerous nanoparticles results in a mixed microstructure, producing two arcs. However, these arcs are less pronounced in the Cole-Cole plots. The two arcs in the Cole-Cole plots confirm that electrical conduction occurs via both grains and grain boundaries. All plots display partial relaxation associated with the relaxation strength [33-35]. Furthermore, the centers of the arcs for x = 0.1 to 0.7 are positioned along the M'-axis, confirming the presence of non-Debye type relaxations in the ZLTO nanoparticles [33].

The Z'-log f and Z"-log f plots provide insights into space charge effects as well as grain and grain boundary behaviors. As shown in Fig. 9a, both Z' and Z" parameters for ZLTO nanoparticles display peak values at low log f. This high magnitude is typically attributed to the influence of grain boundaries, inhomogeneous dielectric structures, and space charge polarization. However, for x = 0.1, the Z' and Z" values are notably lower due to the presence of electron-pinned defect dipoles [35]. At higher log f values, Z' and Z" increase, reflecting the enhance carrier movement within the grains of the polycrystalline material. This increase results in higher electrical conductivity due to the predominant mobility of the charge carriers. In contrast, x = 0.1 shows lower Z' and Z" values at high log f, which can be attributed to the smaller number of grain boundaries present in its nanoparticle-like structure. The relaxation frequencies increase with log f, ranging from 2.4612 to 2.8142 and from 2.4771 to 2.9542 for x = 0.1 to 0.7, respectively, as shown in the Z'-log f and Z"-log f plots. Additionally, the Cole-Cole plots (Fig. 9b) illustrate single semicircular arcs for all compositions (x = 0.1-0.7). These arcs indicate partial relaxations due to the charge carriers' long-range mobility [35]. The presence of single arcs suggests that the ZLTO nanoparticles primarily exhibit grain

contributions rather than grain boundary effects, owing to the predominantly nanoparticle-like microstructure with fewer grain boundaries. The arcs below the Z'-axis in the Cole-Cole plots further confirm the occurrence of non-Debye type relaxations in the ZLTO nanoparticles [35].

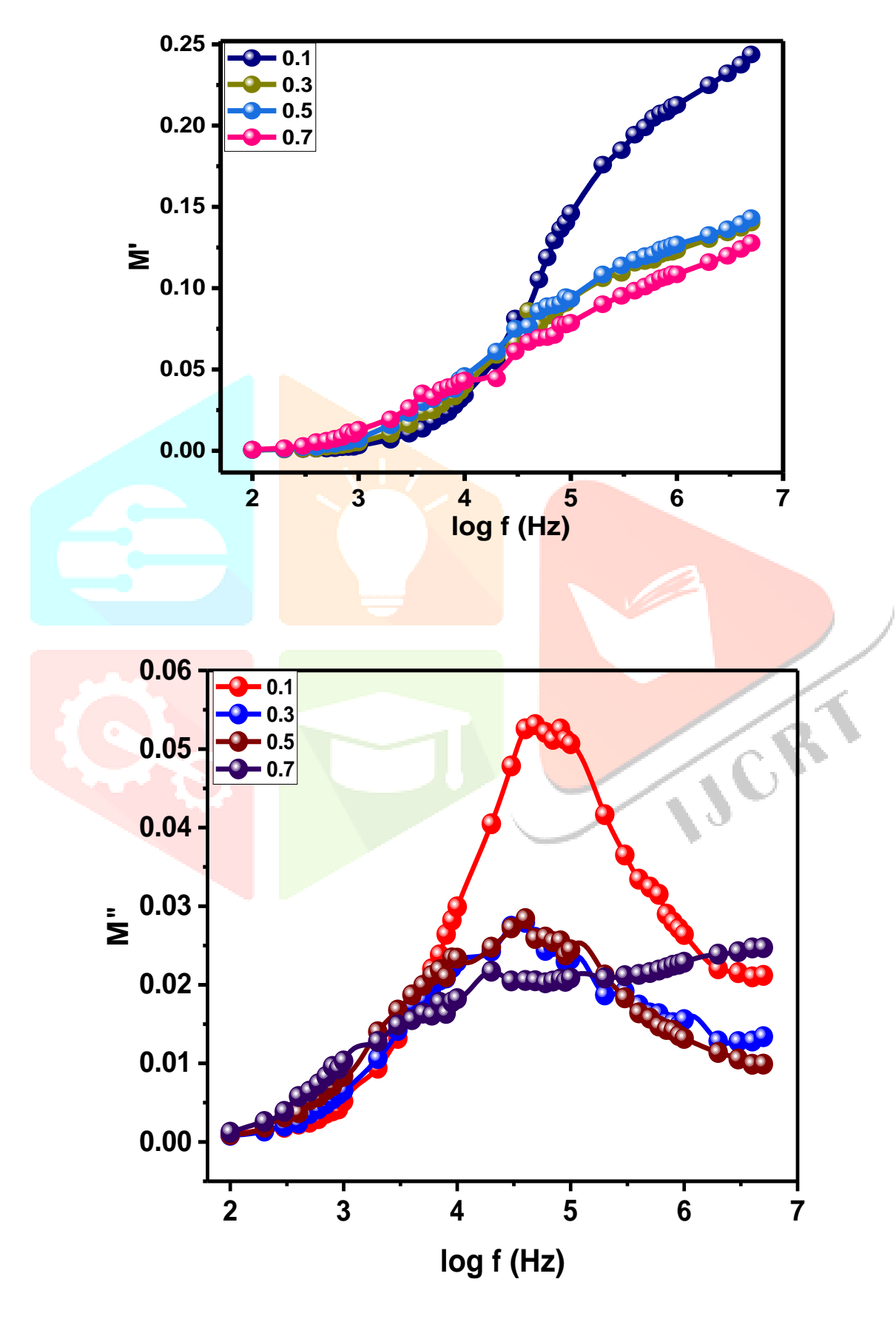


Fig.8a. Frequency dependence of M' and M" of ZLTO nanoparticles

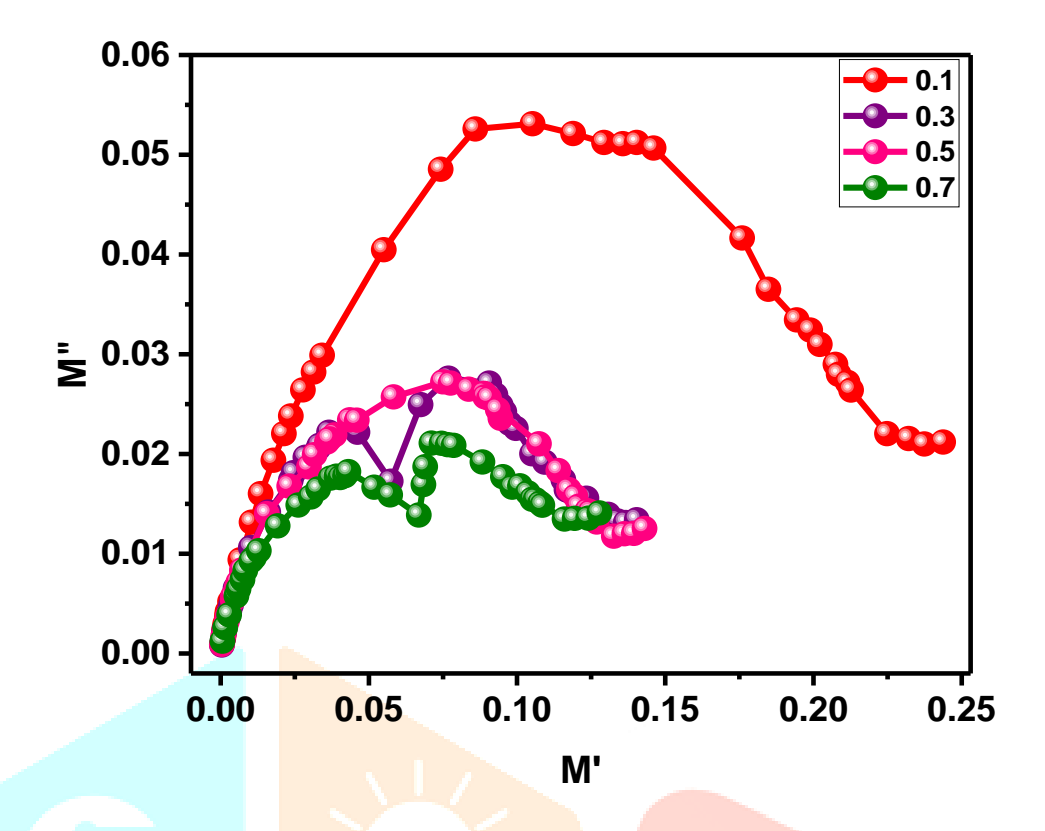
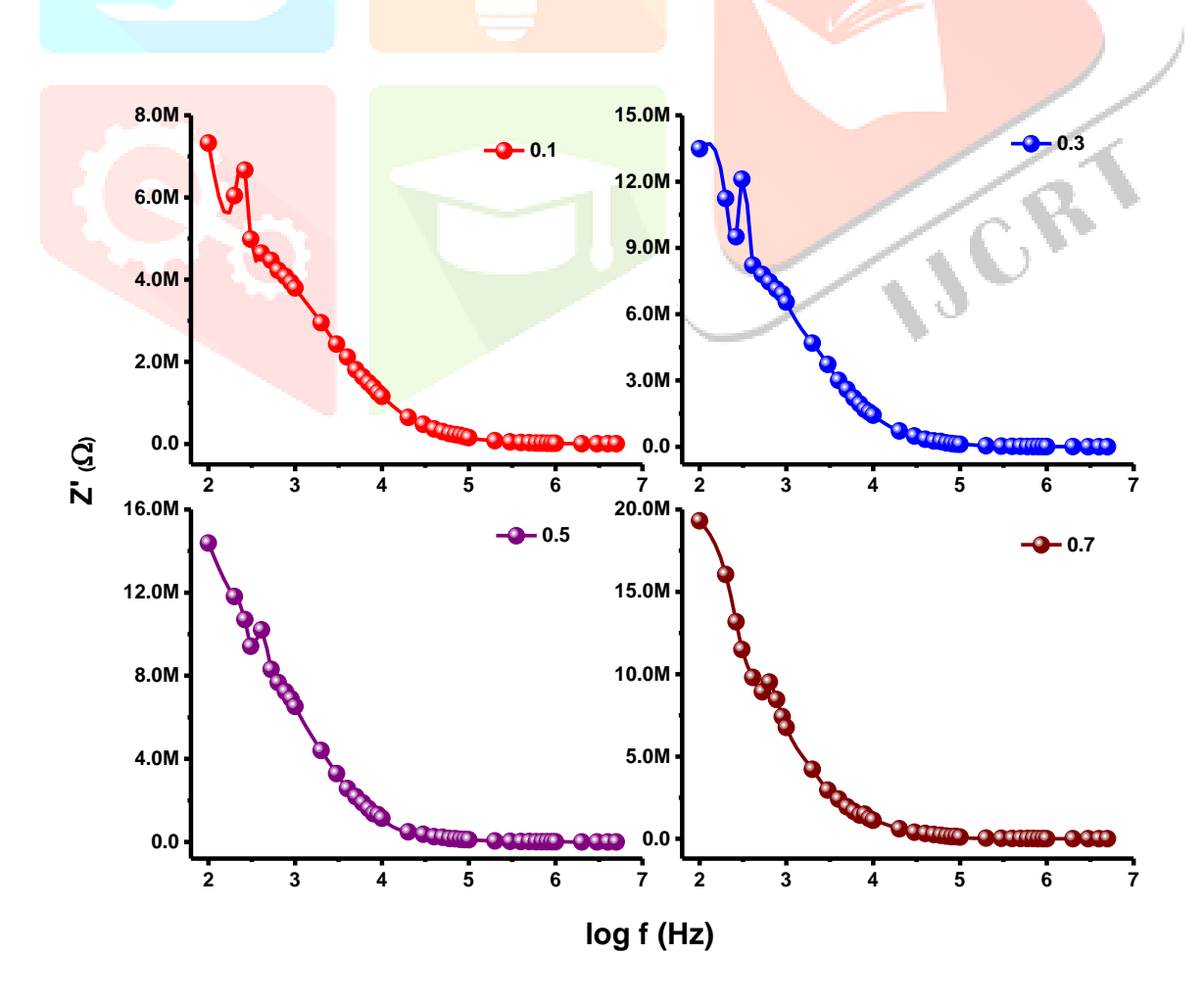


Fig.8b. The Cole-Cole plots M' versus M" plots of ZLTO nanoparticles



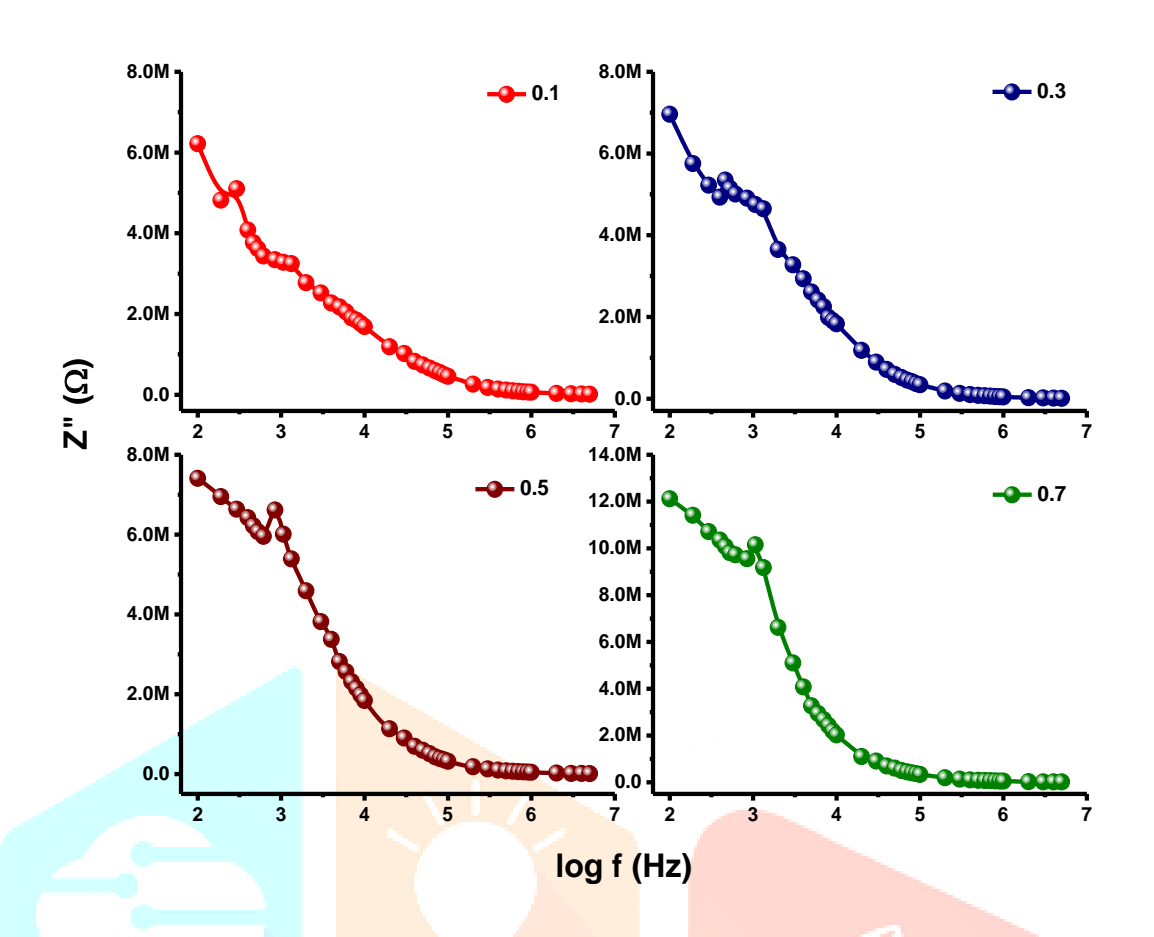


Fig.9a. Frequency dependence of Z' and Z" of ZLTO nanoparticles

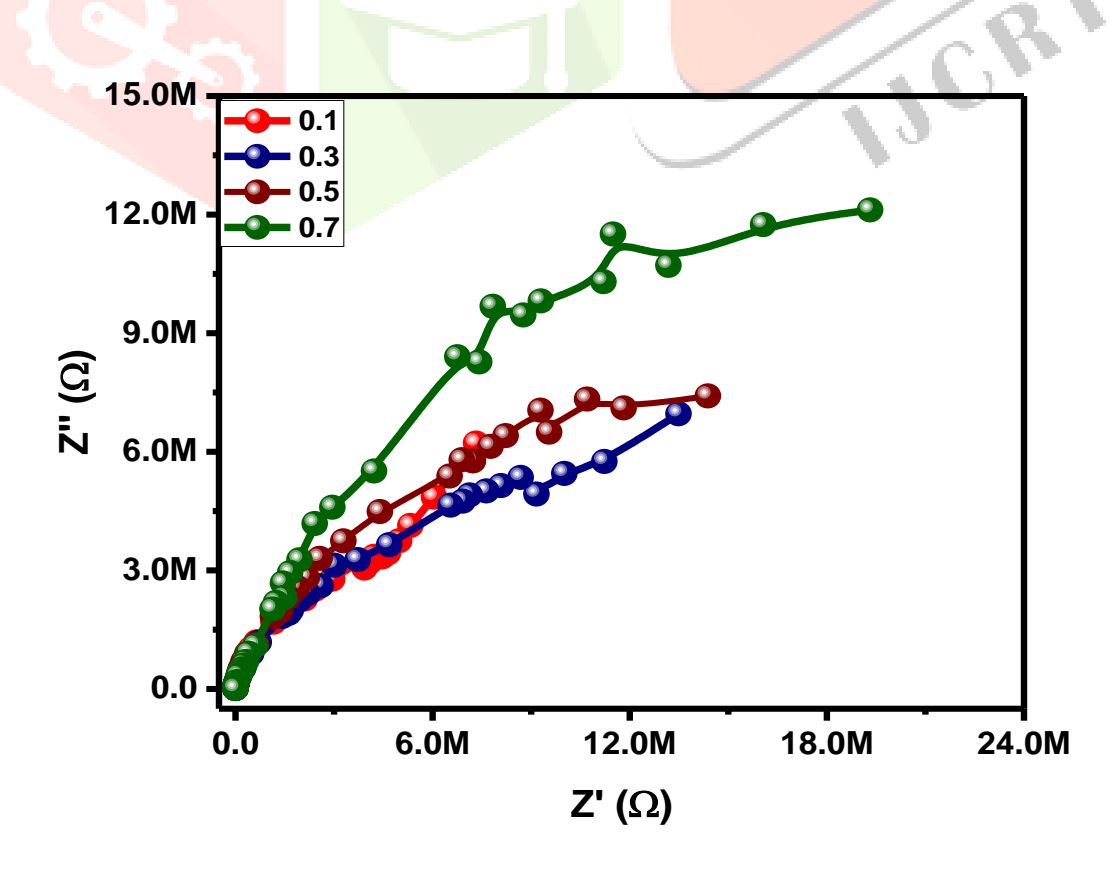


Fig. 9b. The Cole-Cole plots Z' versus Z" plots of ZLTO nanoparticles

#### 4. CONCLUSIONS

Zinc-substituted LaTiO<sub>3</sub> with the composition  $Zn_xLa_{1-x}TiO_3$  (where x=0.1-0.7) was successfully synthesized using a hydrothermal technique. The X-ray diffraction (XRD) patterns were consistent with the standard reference pattern from JCPDS card (89-7507). The observed lattice parameters ranged from a = 3.843 to 3.921 Å and c=27.176 to 27.718 Å. Both the lattice parameters and the crystallite size increased with higher zinc content, with the crystallite size varying from 24.11 to 28.58 nm. Infrared spectroscopy revealed characteristic bands at 540–550 cm<sup>-1</sup> ( $v_a$ ) and 447–457 cm<sup>-1</sup> ( $v_b$ ), confirming the formation of a tetragonal perovskite structure. Dielectric measurements showed that the dielectric constant and dielectric loss ranged from approximately 328 to 494 and 645 to 920, respectively, for x=0.1-0.7 at 100 Hz. The Cole-Cole plots provided insight into the grain and grain boundary resistivity. Analysis of the dielectric modulus and impedance indicated the presence of non-Debye relaxation for all the ZLTO nanoparticles. These optimized dielectric properties suggest that the synthesized materials are well-suited for energy storage applications.

# **ACKNOWLEDGEMENTS**

The authors extend their gratitude to SRMIST Consultancy, Chennai, for facilitating the necessary characterizations, including XRD, FTIR, and UV-Vis. They also acknowledge Yogi Vemana University, YSR Kadapa, for providing SEM with EDAX, and STIC at Cochin University, Kerala, for offering HRTEM with SAED analysis.

#### **REFERENCES**

- 1. C. Srilakshmi, R. Saraf, C. Shiyakumara, Structural Studies of Multifunctional SrTiO<sub>3</sub>Nanocatalyst Synthesized by Microwave and Oxalate Methods: Its Catalytic Application for Condensation, Hydrogenation, and Amination Reactions, ACS Omega 3 (2018) 10503–10512
- 2. I. Zouaria, Z. Sassib, L. Seveyratb, N. Abdelmoulaa, L. Lebrunb, H. Khemakhem, Structural, dielectric, piezoelectric, ferroelectric and electro-caloric properties of Ba<sub>1-x</sub>Ca<sub>x</sub>Ti<sub>0.975</sub>(Nb<sub>0.5</sub>Yb<sub>0.5</sub>)<sub>0.025</sub>O<sub>3</sub> lead-free ceramics, Ceramics International 44 (2018) 8018-8025
- 3. Lee, J.W., Dai, Z., Han, T.H., Choi, C., Chang, S.Y., Lee, S.J. ... Yang, Y, 2D perovskite stabilized phase-pure form amidinium perovskite solar cells. Nature Communications, 9 (2018), doi:10.1038/s41467-018-05454-4
- 4. Ho, K.T., Leung, S.F., Li, T.Y., Maity, P., Cheng, B., Fu, H.C.,... He, J.H., Surface Effect on 2D Hybrid Perovskite Crystals: Perovskites Using an Ethanolamine Organic Layer as an Example. Advanced Materials, (2018) 1804372, doi:10.1002/adma.201804372
- 5. Madhavan, B., & Ashok, A, Dielectric properties of A and B-site doped LaTiO<sub>3-δ</sub>perovskites synthesized by sol-gel method. Journal of Sol-Gel Science and Technology, 73 (2014) 1–8, doi:10.1007/s10971-014-3486-2
- 6. Mozhegorov AA, Nikiforov AE, Larin AV, Efremov AV, Gonchar LE, Agzamova PA, Structure and the electronic and magnetic properties of LaTiO<sub>3</sub>Phys Solid State 50 (2008) 1795–1798
- 7. Ishida H, Liebsch A, Origin of metallicity of LaTiO<sub>3</sub>/SrTiO<sub>3</sub>heterostructures, Phys Rev B 77 (2008) 115350
- 8. Bradha, M., Hussain, S., Chakravarty, S., Amarendra, G., & Ashok, A, Synthesis, structure and total conductivity of A-site doped LaTiO<sub>3-δ</sub>perovskites. Journal of Alloys and Compounds, 626 (2015) 245–251
- 9. Arao, M., Inoue, Y., & Koyama, Y, Features of the Jahn–Teller displacements in LaTiO<sub>3</sub>, Journal of Physics and Chemistry of Solids, 63 (2002) 995–997
- 10. Havelia, S., Balasubramaniam, K. R., Spurgeon, S., Cormack, F., & Salvador, P. A., Growth of La<sub>2</sub>Ti<sub>2</sub>O<sub>7</sub> and LaTiO<sub>3</sub> thin films using pulsed laser deposition. Journal of Crystal Growth, 310 (2008) 1985–1990
- 11. Herrera, G., Jiménez-Mier, J., &Chavira, E., Layered-structural monoclinic-orthorhombic perovskite La<sub>2</sub>Ti<sub>2</sub>O<sub>7</sub> to orthorhombic LaTiO<sub>3</sub> phase transition and their microstructure characterization. Materials Characterization, 89 (2014)13–22
- 12. Wang, Y., Zhong, H., Li, X., Jia, F., Shi, Y., Zhang, W.,... Wang, J., Perovskite LaTiO<sub>3</sub>–Ag<sub>0.2</sub>nanomaterials for nonenzymatic glucose sensor with high performance. Biosensors and Bioelectronics, 48 (2013) 56–60
- 13. Jia, F.F., Zhong, H., Zhang, W.G., Li, X.-R., Wang, G.Y., Song, J.,...Guo, L. P., A novel nonenzymatic ECL glucose sensor based on perovskite LaTiO<sub>3</sub>-Ag<sub>0.1</sub>nanomaterials. Sensors and Actuators B: Chemical, 212 (2015) 174–182

- 14. Chen, Y., Xu, J., Cui, Y., Shang, G., Qian, J., & Yao, J., Improvements of dielectric properties of Cu doped LaTiO<sub>3+δ</sub>. Progress in Natural Science: Materials International, 26 (2016) 158–162
- 15. Zhang, L., Nie, Y., Hu, C., &Qu, J., Enhanced Fenton degradation of Rhodamine B over nanoscaled Cu-doped LaTiO<sub>3</sub>perovskite. Applied Catalysis B: Environmental, 125 (2012) 418–424
- 16. Mkhalid, I. A., Visible light photocatalytic synthesis of aniline with an Au/LaTiO<sub>3</sub>nanocomposites. Journal of Alloys and Compounds, 631 (2015) 298–302
- 17. Rakibuddin, M., Kim, H., &Ehtisham Khan, M., Graphite-like carbon nitride (C<sub>3</sub>N<sub>4</sub>) modified N-doped LaTiO 3 nanocomposite for higher visible light photocatalytic and photo-electrochemical performance. Applied Surface Science, 452 (2018) 400–412
- 18. Marozau, I., Shkabko, A., Döbeli, M., Lippert, T., Mallepell, M., Schneider, C. W.,...Wokaun, A., Pulsed laser deposition and characterisation of perovskite-type LaTiO<sub>3-x</sub>N<sub>x</sub> thin films. ActaMaterialia, 59 (2011) 7145 7154
- 19. Vilquin, B., Kanki, T., Yanagida, T., Tanaka, H., & Kawai, T., Control of p-type conductivity in Sr doped LaTiO<sub>3</sub> thin films. Solid State Communications, 136 (2005) 328 –332
- 20. Goral, J. P., &Greedan, J. E., The magnetic structures of LaTiO<sub>3</sub> and CeTiO<sub>3</sub>, Journal of Magnetism and Magnetic Materials, 37 (1983) 315 321
- 21. Bradha, M., Vijayaraghavan, T., Suriyaraj, S. P., Selvakumar, R., & Ashok, A. M., Synthesis of photocatalytic  $La_{1-x}A_xTiO_{3.5-\delta}$  (A = Ba, Sr, Ca) nanoperovskites and their application for photocatalytic oxidation of congo red dye in aqueous solution. Journal of Rare Earths 33 (2015) 160–167
- 22. Santos, A. G., Leite, J. O., Souza, M. J. B., Gimenez, I. F., &Pedrosa, A. M. G., Effect of the metal type in perovskites prepared by modified proteic method in dye adsorption from aqueous medium. Ceramics International, 44 (2018) 5743 5750
- 23. Sahu K, Murty VVS, Novel sol-gel method of synthesis of pure and aluminium doped TiO<sub>2</sub> nanoparticles, Indian Journal of Pure & Applied Physics 54 (2016) 485 488
- 24. Azarniya, A., Azarniya, A., Hosseini, H. R. M., &Simchi, A, Nanostructured aluminium titanate (Al<sub>2</sub>TiO<sub>5</sub>) particles and nanofibers: Synthesis and mechanism of microstructural evolution. Materials Characterization, 103 (2015) 125–132
- 25. Bakhshandeh, F., Azarniya, A., MadaahHosseini, H. R., &Jafari, S, Are aluminium titanate-based nanostructures new photocatalytic materials? Possibilities and perspectives, Journal of Photochemistry and Photobiology A: Chemistry, 353 (2018) 316 –324
- 26. Ewais, E. M. M., Besisa, N. H. A., & Ahmed A, Aluminumtitanate based ceramics from aluminum sludge waste. Ceramics International, 43 (2017) 10277 10287
- 27. Tang, H., He, J., &Persello, J., Giant electro rheological effects of aluminum-doped TiO<sub>2</sub> nanoparticles. Particuology, 8 (2010) 442 446
- 28. Scherrer, P. Bestimmung der Grosse und der InnerenStruktur von KolloidteilchenMittelsRontgenstrahlen, Nachrichten von der Gesellschaft der Wissenschaften, Gottingen. Mathematisch-PhysikalischeKlasse, 2 (1918) 98-100
- 29. R.D. Shannon, Revised Effective Ionic Radii and Systematic Studies of Interatomic Distances in Halides and Chalcogenides, *ActaCryst.* **A 32** (1976) 751-767.
- 30. C. G. Koops, On the Dispersion of Resistivity and Dielectric Constant of Some Semiconductors at Audio frequencies, Physical Review 83 (1951) 121-124
- 31. K.W. Wagner, The Distribution of Relaxation Times in Typical Dielectrics, Ann. Phys., 40 (1913) 817
- 32. M A Ell Hiti, AC. electrical conductivity of Ni–Mg ferrites, J. Phys. D: Appl. Phys. 29 (1996) 501–505.
- 33. Mansour S F, Abdo M A, and Alwan S M, The role of Cr<sup>3+</sup> ions substitution on structural, magnetic and dielectric modulus of manganese zinc nanoferrites Ceram. Int. 44 (2018), 8035–42
- 34. Bhaskar Reddy S, Prasad Rao Kand, Ramachandra Rao M S, Effect of La substitution on the structural and dielectric properties of BaZr<sub>0.1</sub>Ti<sub>0.9</sub>O<sub>3</sub> ceramics J. Alloys Compd. 481 (2009) 692–6
- 35. S. Dastagiri, M. V. Lakshmaiah, K. Chandra Babu Naidu, Defect dipole polarization mechanism in low-dimensional Europium substituted Al<sub>0.8</sub>La<sub>0.2</sub>TiO<sub>3</sub> nanostructures, Physica E: Low-dimensional Systems and Nanostructures 120 (2020) 114058
- 36. N. Raghuram, T. S. Rao, K. Chandra Babu Naidu. Investigations on Functional Properties of Hydrothermally Synthesized Ba<sub>1-x</sub>Sr<sub>x</sub>Fe<sub>12</sub>O<sub>19</sub>(x= 0.0 0.8) Nanoparticles, Material Science in Semiconductor Processing 94, (2019), 136-150

- 37. T. M. Hammad, S.Kuhn, A. A. Amsha, et.al., Comprehensive Study of the Impact of Mg<sup>2+</sup> Doping on Optical, Structural, and Magnetic Properties of Copper Nanoferrites. Journal of Superconductivity and Novel Magnetism. (2020), doi:10.1007/s10948-020-05559-2
- 38. Li Zhang, Dezhi Qin, Guangrui Yang, Qiuxia Zhang, The Investigation on synthesis and optical properties of ZnS:Conanocrystals by using hydrothermal method, Chalcogenide Letters, Vol. 9, No. 3, (2012), p. 93 98
- 39. Chao-Wei Huang, Rou-An Chen, Wei-Yu Chen, et.al., Manipulating and Revealing the Roles of La and Zr Dopants into ZnTiO<sub>3</sub>Perovskite Toward Heterogeneous Photocatalytic Degradation of Tetracycline Under Visible Light Irradiation, Topics in Catalysis, (2022) https://doi.org/10.1007/s11244-022-01616-3
- 40. Abdeen, A. Electric conduction in Ni–Zn ferrites. Journal of Magnetism and Magnetic Materials, 185(2), (1998) 199–206. doi:10.1016/s0304-8853(97)01144-x

